

Original article

Evaluation of bedding effect on the bursting liability of coal and coal-rock combination under different bedding dip angles

Chao Wang^{1,2}, Yv Liu¹, Dazhao Song³, Jianhui Xu¹✉*, Qiwei Wang¹, Shaoyuan Zhang¹

¹Faculty of Land Resources Engineering, Kunming University of Science and Technology, Kunming 650093, P. R. China

²Key Laboratory of Mine Thermodynamic Disasters and Control of Ministry of Education (Liaoning Technical University), Huludao 125105, P. R. China

³School of Civil and Resource Engineering, University of Science and Technology Beijing, Beijing 100083, P. R. China

Keywords:

Rock burst
bursting liability
light gradient boosting machine model
particle flow code
bedding effect

Cited as:

Wang, C., Liu, Y., Song, D., Xu, J., Wang, Q., Zhang, S. Evaluation of bedding effect on the bursting liability of coal and coal-rock combination under different bedding dip angles. *Advances in Geo-Energy Research*, 2024, 11(1): 29-40. <https://doi.org/10.46690/ager.2024.01.04>

Abstract:

Rock bursts pose a significant risk to coal mine operation safety. Thus, accurately discriminating coal bursting liabilities is crucial for predicting and preventing rock burst events. To better understand the effects of a varying bedding angle on the crack propagation rule, failure mode and bursting liability level of coal and coal-rock combinations, we propose an optimized machine learning-based model. Additionally, uniaxial compressive tests are conducted using PFC3D software on samples with different bedding angles. The results indicate that, among the nine light gradient boosting machine discriminant models constructed using three data preprocessing methods and three parameter optimization algorithms, the optimal model is identified as the particle swarm optimization-light gradient boosting machine discriminant model based on Z-score standardization method, which exhibits the best stability and has a F1-score of 93.6%. Bedding has a significant impact on the failure modes of two kinds of samples, resulting in an evident bedding effect on their bursting liability. The uniaxial compression strength and bursting energy index of both samples show a reduction-rising trend with an increasing bedding dip angle. However, the bursting liability level of these samples is not affected by 0° or 90° bedding dip angle. Therefore, when assessing the bursting liability of samples, the influence of coal seam bedding and its dip angles should be thoroughly considered.

1. Introduction

A dynamic disaster in coal mines known as “rock burst” occurs when coal-rock masses around a mine roadway or working face suddenly and violently fail due to a rapid discharge of elastic energy (He et al., 2019; Frith et al., 2020; Chen et al., 2022; Ali et al., 2023; Liu et al., 2023; Peng et al., 2023). Such events seriously jeopardize the security of mining operations (Khan et al., 2022; He et al., 2023a; Vardar et al., 2023). Numerous factors contribute to rock burst, one crucial factor being the bursting liability of coal and coal-rock combinations. Bursting liability refers to the property of coal or coal-rock samples of accumulating deformation energy and producing instantaneous impact damage. As coal is a rock mass with well-developed bedding planes, its bursting

liability is significantly influenced by these planes. Therefore, the bursting liability of samples containing bedding planes needs to be precisely assessed for a scientifically based and effective prevention and control of rock bursts (Mark and Gauna, 2016; Vardar et al., 2018; Mottahedi and Ataei, 2019; Zhang et al., 2021).

In recent decades, scholars have extensively explored methods for assessing the bursting liability level of coal as well as the factors influencing the bursting liability of coal and coal-rock samples (He et al., 2023b; Li et al., 2023; Qiu et al., 2023). For instance, regarding the assessment of the bursting liability level, the Chinese national standard “GB/T 25217.2-2010 Classification and laboratory test method on the bursting liability of coal” utilizes the dynamic failure time

index (D_t), elastic strain energy index (W_{et}), bursting energy index (K_e), and uniaxial compression strength (R_c) as evaluation indexes and classifies the bursting liability into level I (strong), level II (weak), and level III (no). Based on the above, fuzzy mathematics were used to determine the assessment level for 73 combinations of evaluation indexes, while the remaining 8 combinations were not explicitly categorized.

The influence of various factors such as temperature, water and gas on the mechanical response characteristics of coal and bursting liability have been studied extensively (Liu et al., 2017; Muhammad et al., 2023). Additionally, research on bedding has also made substantial progress. Regarding the impact of bedding planes and other structural deficiencies, Yang et al. (1998) found that the failure mechanisms of jointed rock masses depend on the angle between bedding planes and maximum principal stress as well as the confining pressure. According to numerical simulations by Bidgoli et al. (2013), the behavior of deformation in cracked rock follows an elastic-plastic model with strain hardening tendencies and the strength of the rock increases with rising confining pressure. Based on the laboratory testing data of hard coal samples, Hao et al. (2016) concluded that coal samples exhibit strong bursting liability at a bedding angle of 0° , weak bursting liability in some cases at 45° and weak bursting liability at 90° for all samples. Mou et al. (2020) discovered a significant effect of the angle between loading direction and joint planes on the mechanical properties of coal samples: With increasing angle, the peak load and failure time exhibited a decreasing trend, followed by an increasing trend.

As demonstrated above, the existing methods for assessing the bursting liability neglect the influence of bedding planes and dip angles, potentially resulting in discrepancies between the assessment results and actual conditions. As such, the current research lacks a systematic comparison of microcrack distribution patterns in coal and coal-rock combinations with varying bedding dip angles, failure modes under loading and the impact of bedding planes on bursting liability. Thus, this study employs a combination of machine learning modeling, numerical simulation and theoretical analysis to develop a bursting liability discriminant model. It systematically investigates the effects of bedding planes with five angles (0° , 30° , 45° , 60° , and 90°) on the sample bursting liability, with the aim to provide guidance for improving methods of bursting liability level assessment.

2. Optimal selection of LightGBM models

The performance of coal bursting liability classification is directly affected by the selection of discriminant indexes and models. In 2017, Microsoft presented a novel training technique known as the Light Gradient Boosting Machine (LightGBM) algorithm, which brought benefits including great accuracy, low memory usage and quick training speed. However, it has not yet been applied to the discriminant of coal bursting liability (Bentejac et al., 2020; Park et al., 2021; Saber et al., 2021; Melsom et al., 2022). Herein, with reference to GB/T 25217.2-2010, a judgment index system is constructed using four indexes: D_t , W_{et} , K_e and R_c . The bursting liability

level is divided into level I (strong), level II (weak) and level III (no).

A sample database of bursting liability was established by widely collecting 152 groups of coal sample data. The samples were split in an 8:2 ratio between training and test set. To find the ideal parameters, five-fold cross-validation was applied to the training set. To eliminate the influence of index dimensionality, three techniques for preprocessing data, namely, min-max normalization, Z-score normalization and centralization, were selected to process the index data of the samples. To optimize the parameters of the LightGBM discriminant model, the genetic algorithm (GA) (Inage et al., 2024), particle swarm optimization (PSO) (Sabzadeh et al., 2020), and simulated annealing (SA) (Sakamoto et al., 2019) were used as three optimization algorithms. Nine LightGBM models were constructed, and the most suitable model was chosen by the comprehensive consideration of F1-score and model stability. The flowchart of the LightGBM model optimization process is shown in Fig. 1.

The F1-score of the nine LightGBM discriminant models is presented in Table 1. The PSO-LightGBM model with Z-score normalization method has the highest F1-score (93.6%), demonstrating strong stability. Therefore, this model was selected as the optimal model.

3. Bedding dip angle influence on coal bursting liability

Due to the changes in sample characteristics and some physical and mechanical properties caused by sampling, transportation and processing in traditional physical mechanical tests, this paper uses PFC3D software to conduct numerical simulation tests and study the failure modes and microcrack propagation distribution rules of coal samples with different dip angles (0° , 30° , 45° , 60° and 90°), as well as to demonstrate how the coal bursting liability is affected by dip angles.

3.1 Establishment of the coal sample model

As coal is a heterogeneous rock material, the parallel bonded contact model in PFC3D software is utilized to install the complete sample particles and the bedding planes are installed using a smooth joint contact model (Chiu et al., 2013; Lambert and Coll, 2014; Potyondy and Cundall, 2014; Park et al., 2018). A complete model of particles with a cylindrical size of 50 mm \times 100 mm (diameter \times height) is established using linearly parallel bonded contacts. Then, different sizes of spherical particles (Ball) with random seed 10,001 are generated in this area. The model contains 8,182 spherical particles and 22,416 contacts, has a porosity of 0.36, a particle size ratio of 1.5, a minimum particle radius of 1.20 mm, and a density of 1,300 kg/m³. In addition, smooth frictionless contact is applied between particles and walls as well as between particles.

Three coal samples were selected from the literature (Yang et al., 2021), with the values of their bursting liability indexes presented in Table 2. The coal bursting liability level was assessed using the PSO-LightGBM model created in this work,

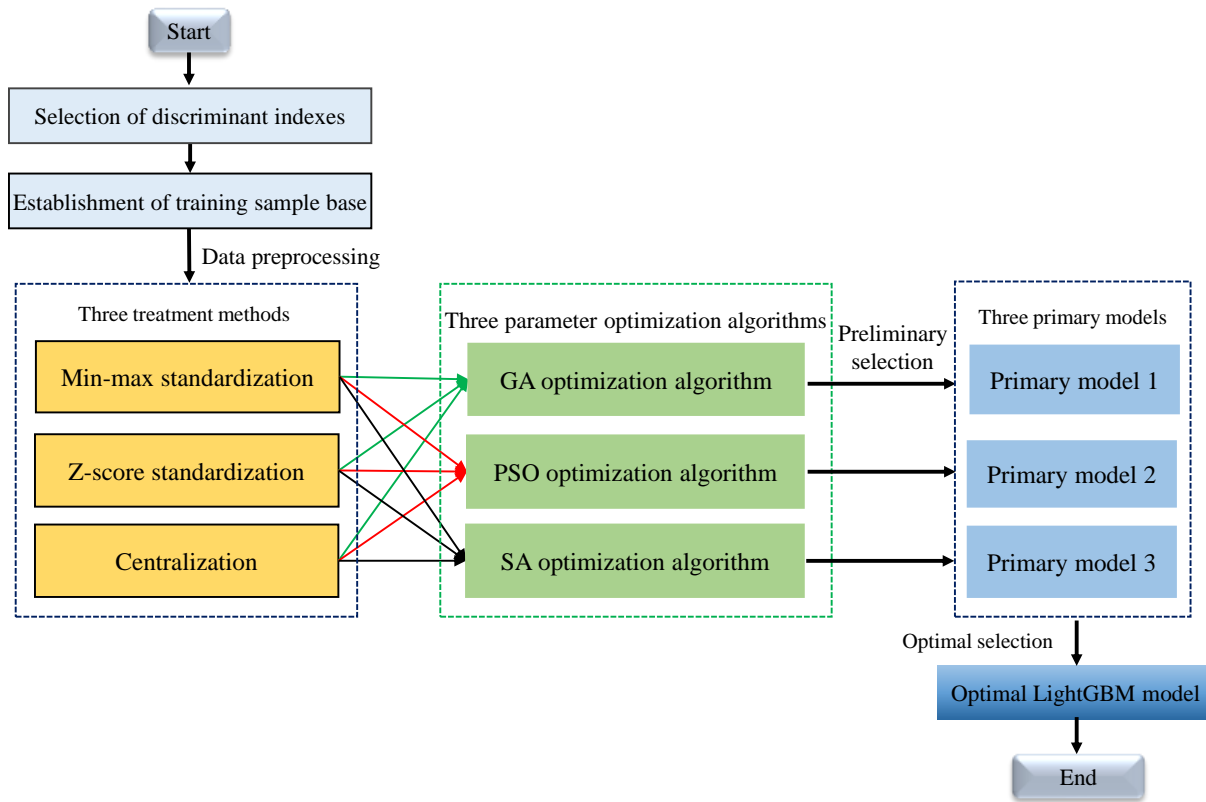


Fig. 1. Flowchart of the optimization process.

Table 1. F1-score (%).

Model	Min-max normalization method	Z-score normalization method	Centralization method
GA-LightGBM	87.8	91.7	79.7
PSO-LightGBM	84.7	93.6	86.1
SA-LightGBM	75.6	86.6	85.6

Table 2. Discriminant indexes and results of bursting liability level for coal sample.

No.	Discriminant indexes				Bursting liability level
	D_t (ms)	W_{et} (-)	K_e (-)	R_c (MPa)	
1	52	7.22	5.15	33.23	I
2	359	4.14	1.97	11.93	II
3	1130	1.89	1.33	5.24	III

and the output of the model was entirely compatible with the discriminant outcomes by the Chinese national standard.

The micro-parameters of the three types of samples with strong, weak and no bursting liability (referred to as sample A, B and C, respectively) are shown in Table 3.

Bedding is a structure formed within a layer during the sedimentation process, mainly displayed by the vertical changes of sediment composition, structure, color, and others. Therefore, as mentioned earlier, the smooth joint model is installed

on the bedding planes of samples, and the normal stiffness (s_j -kn), tangential stiffness (s_j -ks) and friction coefficient (s_j -fa) of the smooth joint model are calibrated as micro-parameters of the bedding planes. After repeated calibration, the micro-parameters are presented in Table 4.

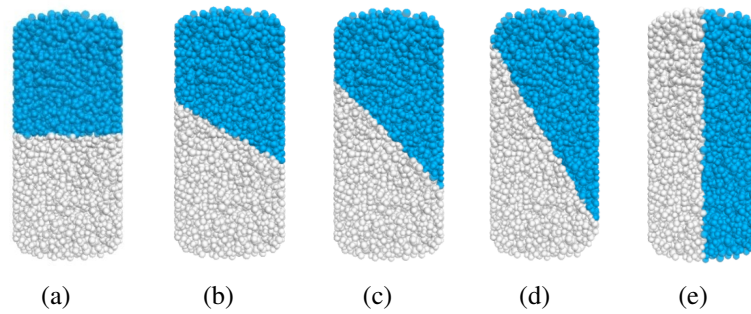
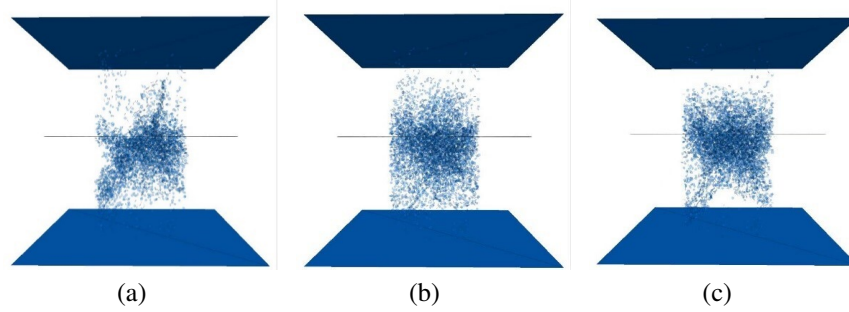
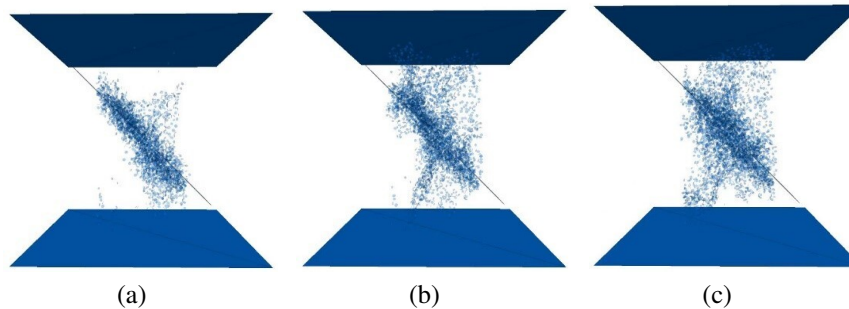
The models with different angles are shown in Fig. 2. Uniaxial compressive experiments of coal samples were simulated by placing loading on the upper surface of the model, with the loading rate of 0.005 mm/s.

Uniaxial compressive tests were conducted on coal samples containing bedding planes with different angles to obtain microcrack distribution maps. Three representative bedding angles of 0° , 45° and 60° were selected for analysis, and the microcrack distribution of coal samples is shown in Figs. 3 to 5.

When $\theta = 0^\circ$, the particle damage, displacement and microcracks are mainly concentrated in the middle, with a small amount produced at the ends of the sample (see Fig. 3). The connected cracks form smaller shattered particles. Sample A produces fewer shattered particles, while sample C yields

Table 3. Microscopic parameters of coal samples.

Parameter	FISH language	Sample A	Sample B	Sample C
Contact modulus (GPa)	emod	1.73	1.37	0.80
Contact stiffness ratio (-)	kratio	2	2	2
Parallel bond modulus (GPa)	pb-emod	1.73	1.37	0.80
Parallel bond stiffness ratio (-)	pb-kratio	2	2	2
Normal bond strength (MPa)	pb-ten	[20.2, 21.2]	[8.7, 9.7]	[3.8, 4.2]
Tangential bond strength (MPa)	pb-coh	[40.9, 41.9]	[17.9, 18.9]	[7.8, 8.2]
Internal friction angle (°)	pb-fa	0	20	40

**Fig. 2.** Coal sample model with different angles θ . (a) 0° , (b) 30° , (c) 45° , (d) 60° and (e) 90° .**Fig. 3.** Microcrack distribution of coal samples when $\theta = 0^\circ$. (a) Sample A, (b) B and (c) C.**Fig. 4.** Microcrack distribution of coal samples when $\theta = 45^\circ$. (a) Sample A, (b) B and (c) C.

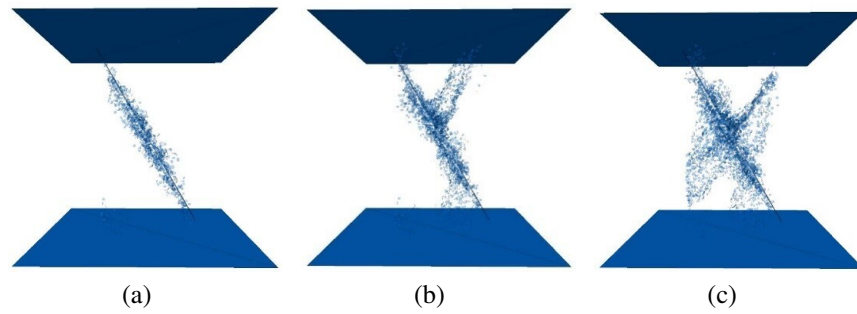


Fig. 5. Microcrack distribution of coal samples when $\theta = 60^\circ$. (a) Sample A, (b) B and (c) C.

Table 4. Microscopic parameters of the smooth bedding model in coal samples.

Parameter	FISH language	Parameter value
Normal stiffness (GPa)	sj-kn	1.3
Shear stiffness (GPa)	sj-ks	1.4
Friction coefficient (-)	sj-fa	0.1

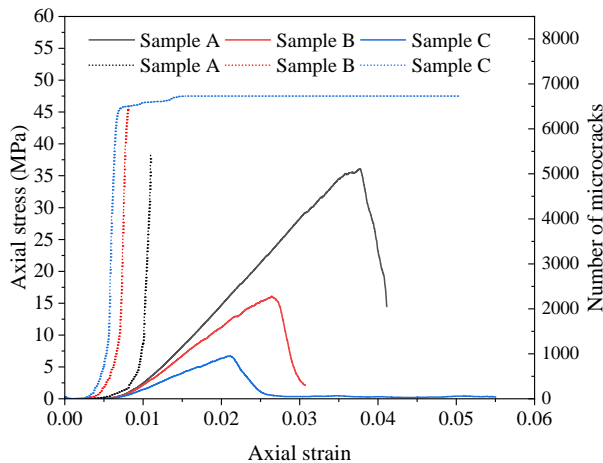


Fig. 6. Stress-strain and microcrack number curves of samples when $\theta = 0^\circ$.

more shattered particles, forming larger shattered blocks and resulting in larger compression deformation in the middle of the sample (i.e., bedding planes).

When $\theta = 45^\circ$, a small number of shattered particles detach from all coal samples and significant displacements occur along the bedding planes (see Fig. 4). The microcracks mainly develop along the bedding planes, with only a few microcracks appearing at the loading ends. In sample A, there are fewer microcracks intersecting with the bedding planes and the destruction mainly occurs along the bedding planes. In samples B and C, microcracks intersect with the bedding planes and penetrating microcracks form intersecting fracture surfaces with them. This indicates predominantly shear-type failure.

When $\theta = 60^\circ$, the number of microcracks generated after the complete destruction of coal samples is the lowest based

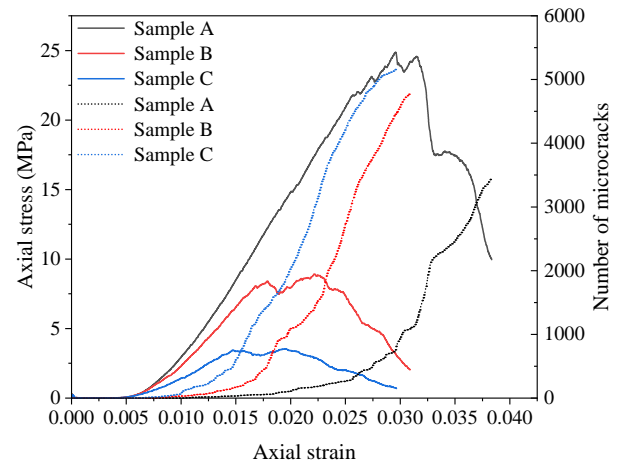


Fig. 7. Stress-strain and microcrack number curves of samples when $\theta = 45^\circ$.

on comparing the subfigures of Fig. 5. Particle fracturing is predominantly oriented along the bedding planes, with the fracture surfaces mainly developing and propagating along them and penetrating through the coal sample. There are almost no microcracks at the loading ends and no significant detachment of shattered particles is observed. In sample A, microcracks are evenly distributed at both ends of the bedding planes without shear failure. On the other hand, samples B and C exhibit fracture surfaces intersecting with the bedding planes, indicating that shear failure has occurred.

The aforementioned results lead to the conclusion that microcracks have a steady propensity to form around the bedding planes as the angle changes from 0° to 60° . The samples show an increasing inclination for slip along the bedding planes, leading to a gradual reduction in compressive strength that in turn impacting the coal bursting liability.

3.2 Analysis of failure modes

Taking $\theta = 0^\circ$, 45° and 60° as examples, the stress-strain curves and microcrack quantities for three types of samples with different angles under uniaxial load are illustrated in Figs. 6 to 8.

The stress-strain curves of three types of samples exhibit a “single peak” shape when $\theta = 0^\circ$ (see Fig. 6). Sample A has the highest uniaxial compressive strength, while sample C has

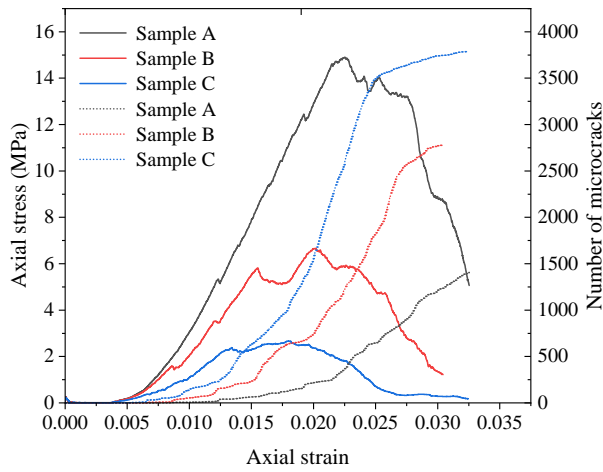


Fig. 8. Stress-strain and microcrack number curves of samples when $\theta = 60^\circ$.

the lowest. During the failure stage, sample A experiences a rapid decrease in stress, leading to brittle fracture, and it still maintains a significant residual strength after complete failure. Sample B undergoes brittle fracture accompanied by plastic failure after reaching the peak strength. Meanwhile, sample C exhibits plastic deformation after reaching the peak strength, with a relatively large proportion of residual strength in the deformation stage. When comparing the microcrack number curves, it can be observed that sample A has the fewest microcracks. The microcrack number increases rapidly and reaches its maximum after a certain period of loading, after which no new microcracks form. In contrast, sample C already exhibits microcracks in the initial stage and the number of microcracks increases rapidly during the loading process, eventually reaching a plateau and remaining relatively stable for a longer duration.

The stress-strain curves for $\theta = 45^\circ$ are similar to those for $\theta = 30^\circ$ (see Fig. 7). They exhibit stress yielding before reaching the peak stress and display a “double peak” shape, followed by a step-like oscillating decline afterwards. The rate of stress decrease in the failure stage is relatively slow and all samples undergo plastic failure. Compared with $\theta = 0^\circ$, the number of microcracks at $\theta = 30^\circ$ and $\theta = 45^\circ$ is lower, indicating that the microcracks have penetrated into each other to form large cracks, resulting in a gradually decreasing compressive strength of the sample. This leads to a progressive reduction in the compressive strength of the samples.

When $\theta = 60^\circ$, the coal samples undergo stress yielding and stress strengthening during the loading process (see Fig. 8). The stress-strain curves exhibit a “double peak” or even a “multi peak” shape, indicating that multiple yield events take place in the samples. This leads to the lowest compressive strength among the five types of samples with different angles. After reaching the peak strength, the curves exhibit a slow step-like decline and all samples undergo plastic failure. According to the microcrack number curves, the coal samples have a smaller number of microcracks. This is due to the merging of larger cracks through the joining of microcracks, resulting in significant damage to the samples.

In light of the above analysis, coal samples with higher

Table 5. Discriminant results of bursting liability levels by the PSO-LightGBM model.

Sample	$\theta(^{\circ})$	R_c (MPa)	K_e (-)	Bursting liability level
A	0	36.09	6.02	I
	30	28.55	3.59	I
	45	24.88	1.77	II
	60	14.90	1.01	II
	90	39.67	6.48	I
B	0	16.07	4.28	II
	30	10.56	1.00	III
	45	8.92	1.69	III
	60	6.66	3.38	III
	90	18.16	3.75	II

uniaxial compression strength exhibit stronger bursting liability, with fewer cracks generated before reaching the yield limit.

3.3 Bedding influence on the coal bursting liability

In the previous part, the impact of bedding planes on the uniaxial compression strength and bursting liability of samples was examined. In this section, to explore the impact of bedding angle on bursting liability, a comparative analysis is conducted on samples with five dip angles. Sample C has no bursting liability, which lacks research significance and will not be included in the comparative analysis. Fig. 9 shows the microcrack number and stress-strain curve of five included samples.

As the dip angle increases, the two kinds of samples with bursting liability show a tendency toward decreasing microcrack number and uniaxial compressive strength, followed by increase (see Fig. 9). Specifically, when the dip angle is 0° or 90° , the samples exhibit a larger microcrack number and compressive strength. The 60° sample exhibits the smallest microcrack number and lowest strength. The R_c and K_e values of five samples, calculated from the stress-strain curve, are presented in Table 5. It is evident that both R_c and K_e values decrease and then rise with the increasing dip angle. By inputting the R_c and K_e values into the PSO-LightGBM discriminant model, the bursting liability level can be determined.

The impact of bedding dip angle on the bursting liability of samples is specifically manifested as follows (see Table 5): (1) For sample A with strong bursting liability, the bursting liability level remains unchanged when $\theta = 0^\circ$, 30° or 90° . When $\theta = 45^\circ$ or 60° , the coal sample transitions from strong to weak bursting liability level. (2) For sample B with weak bursting liability, the level remains unchanged when $\theta = 0^\circ$ or 90° . When $\theta = 30^\circ$, 45° or 60° , the coal sample transitions to no bursting liability.

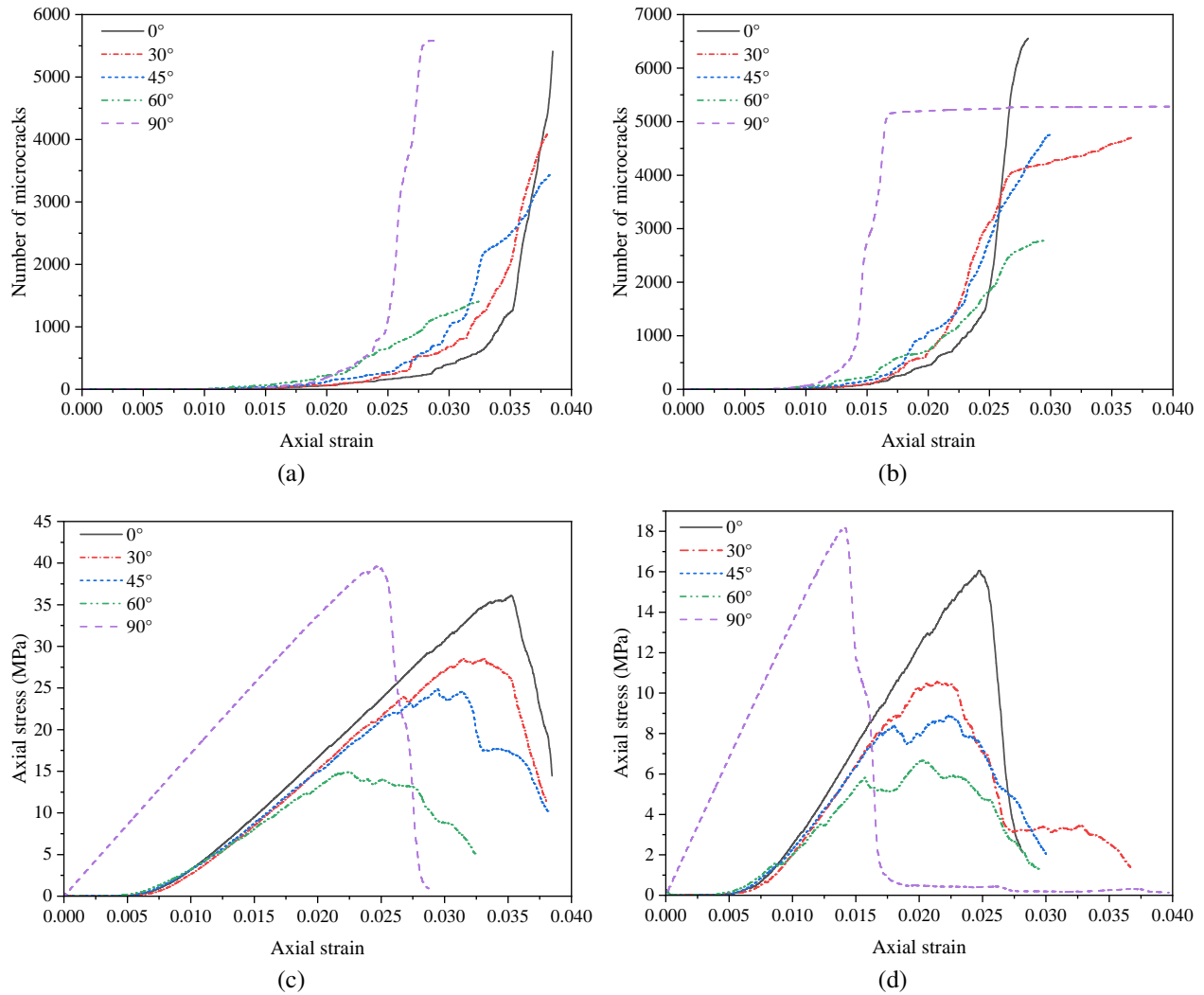


Fig. 9. Microcrack numbers and stress-strain curves of samples. (a) Number of microcracks for sample A (b) and B, (c) Stress-strain curves for sample A and (d) B.

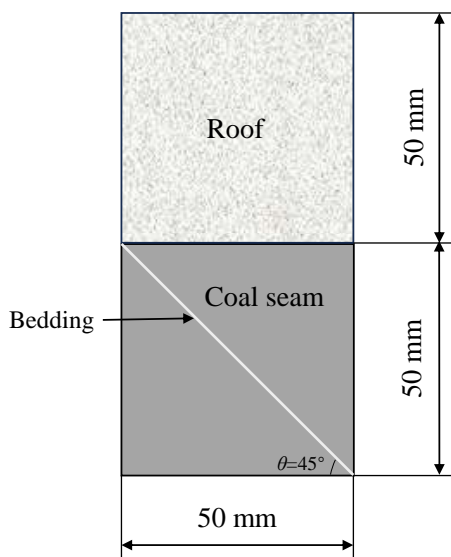


Fig. 10. Model of coal-rock combination sample ($\theta = 45^\circ$).

4. Bedding dip angle on coal-rock combination

4.1 Establishment of a combination sample model

According to the determination method outlined in “Classification and laboratory test method on the bursting liability of coal-rock combination sample”, a combination sample model (diameter is 50 mm, length is 100 mm) with a height ratio of 1:1 between rock and coal, was built in PFC3D software and different bedding dip angles were added to the coal sample. Fig. 10 illustrates the sample model with a dip angle of 45° .

Here, the microstructural parameters of the coal samples described in Section 3.1 were selected. Different dip angles were installed in the coal of the combination samples, resulting in combination sample D with strong bursting liability coal and sample E with weak bursting liability coal. For the rock sample in the combination samples, the parallel bonding model was selected. After multiple modifications and adjustments, Table 6 lists the microstructural properties of the acquired rock sample.

Table 6. Microscopic parameters of rock sample.

Parameter	FISH language	Parameter value
Contact modulus (GPa)	emod	7.26
Contact stiffness ratio (-)	kratio	2.2
Parallel bond modulus (GPa)	pb-emod	7.26
Parallel bond stiffness ratio (-)	pb-kratio	2.2
Normal bond strength (MPa)	pb-ten	[39.2, 40.7]
Tangential bond strength (MPa)	pb-coh	[77.9, 79.1]
Internal friction angle (°)	pb-fa	20

The interface between rock and coal was described using a linear contact model.

4.2 Microcrack analysis

In order to obtain the microcrack distribution and particle failure mechanisms following loading, uniaxial compressive tests were performed on two types of two combination samples. Three representative bedding angles of 0°, 45° and 60° were selected for analysis, and the microcrack distribution of samples are shown in Figs. 11 to 13.

When the dip angle $\theta = 0^\circ$ in the coal sample, during the process of uniaxial compressive loading, microcracks first initiate along the bedding planes and develop guided by them (see Fig. 11). As loading continues, the microcracks gradually propagate from the bedding planes to the entire coal sample. Furthermore, because the coal in combination sample D has greater strength, significantly fewer microcracks are observed compared to sample E.

When $\theta = 45^\circ$, during the initial stages of loading, microcracks in the sample develop guided by the bedding planes (see Fig. 12). After loading for a period of time, the microcracks gradually expand radially from the bedding plane to the surrounding area. Upon the completion of loading, microcracks merge and form larger fissures along the bedding planes. Because the microcrack distribution of sample D is denser, significant displacement occurs along the bedding planes during loading. In sample E, microcracks develop along the bedding planes towards the lower right end and they extend to both sides. Fractured bodies are formed after microcracks intersect with each other.

By comparing and analyzing Fig. 13, the combination sample exhibits the most severe damage when $\theta = 60^\circ$. During the initial stages of loading, microcracks in the sample develop independently of the bedding planes, resulting in a large number of microcracks at both ends of the bedding planes. As the loading process progresses, microcracks gradually transition from the ends towards the bedding planes guided by them. Upon the completion of loading, larger cracks occur within the bedding planes of the samples.

4.3 Bedding influence

The previous sections of this paper have indicated that the bedding in coal samples has an impact on the crack distribution, failure mode and compressive strength of combination samples. Thus, this section compares and evaluates the effect of dip angle on the bursting liability of the combination sample. Fig. 14 illustrates the microcrack number and stress-strain curve of samples D and E under uniaxial loading.

The combination sample generates the highest number of microcracks at $\theta = 90^\circ$, followed by 30°, and then 60° (see Fig. 14). When $\theta = 0^\circ$, the sample has the maximum uniaxial compressive strength, followed by 90°. The post-peak stress-strain curve is steep, indicating a stronger escape of energy in the coal sample and a primarily brittle failure mode, implying a higher bursting liability. When $\theta = 30^\circ, 45^\circ$ or 60°, the stress-strain curves are relatively flat and lack a distinct peak. They often exhibit a “double peak” shape, indicating plastic failure. The uniaxial compression strength is lower at this time, indicating a weaker bursting liability for the samples.

In order to better visualize the bursting liability of combination samples impacted by the bedding angle, the R_c and K_e values were derived based on the stress-strain curves of combination samples with varied dip angles (see Fig. 15).

Based on the analysis in Fig. 15, when the bedding dip angle in coal samples increases, both R_c and K_e values of the combination samples exhibit a tendency of lowering initially and then rising. Additionally, combination sample D exhibits higher R_c and K_e values compared to sample E. By incorporating the R_c and K_e values into the PSO-LightGBM discriminant model, the bursting liability levels of the five combination samples were determined. The results of this model show strong agreement with the single-index discriminant results specified in the national standard, as presented in Table 7.

The bedding with different dip angles contained in the coal sample exert different effects on the bursting liability of the combination samples, as listed in Table 7: (1) For sample D, when $\theta = 0^\circ$ or 90°, the sample exhibits strong bursting liability; when $\theta = 30^\circ$, the sample shows weak bursting liability; when 45° or 60°, the sample exhibits no bursting liability. (2) For sample E, when $\theta = 0^\circ$ or 90°, the sample displays weak bursting liability; when 30°, 45° or 60°, the sample shows no bursting liability.

In summary, for the two types of combination samples, the bursting liability levels are unaffected when the bedding dip angles are 0° or 90°. Meanwhile, when $\theta = 30^\circ, 45^\circ$ or 60°, the bursting liability levels of the specimens will reduce to varied degrees.

5. Conclusions

In response to the difficulty in assessing the coal bursting liability level using the eight index combinations specified in the Chinese national standard “Classification and laboratory test method on the bursting liability of coal”, this paper established a PSO-LightGBM model to investigate the microcrack evolution and failure modes of coal and coal-rock samples with different bedding dip angles under uniaxial loading by PFC3D software. Furthermore, the influence of dip angles on

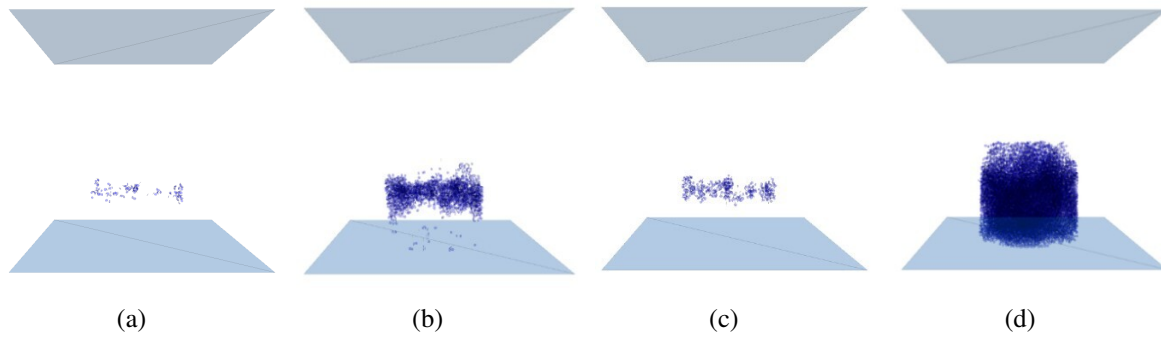


Fig. 11. Microcrack distribution of combination samples when $\theta = 0^\circ$. (a) Sample D at 3 minutes, (b) sample D at 7 minutes, (c) sample E at 3 minutes and (d) sample E at 7 minutes of loading.

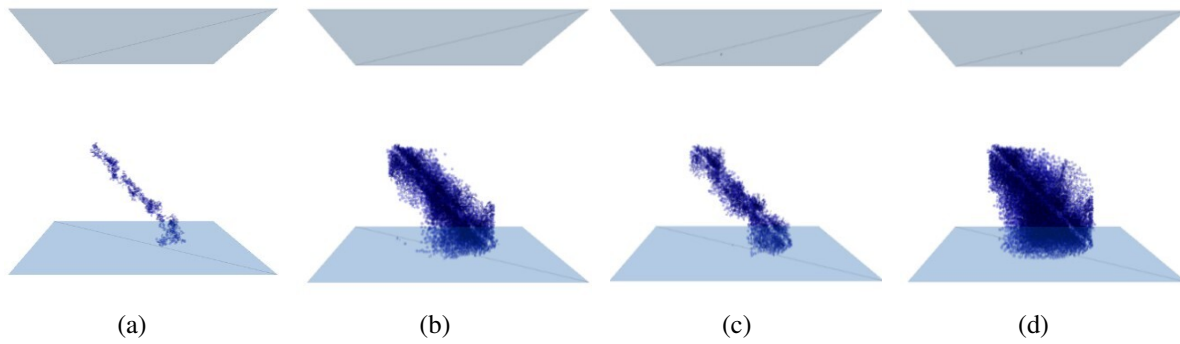


Fig. 12. Microcrack distribution of combination samples when $\theta = 0^\circ$. (a) Sample D at 3 minutes, (b) sample D at 7 minutes, (c) sample E at 3 minutes and (d) sample E at 7 minutes of loading.

Table 7. Bursting liability level of combination samples.

Sample	$\theta(^{\circ})$	R_c (MPa)		K_e (-)		Discriminant level by PSO-LightGBM
		Value	Level	Value	Level	
D	0	20.63	I	5.23	I	I
	30	11.08	II	2.30	II	II
	45	5.39	III	2.07	II	III
	60	6.52	III	1.46	III	III
	90	18.96	I	4.65	II	I
E	0	9.81	II	3.52	II	II
	30	5.46	III	1.33	III	III
	45	4.48	III	0.84	III	III
	60	3.57	III	0.46	III	III
	90	8.87	II	1.65	II	II

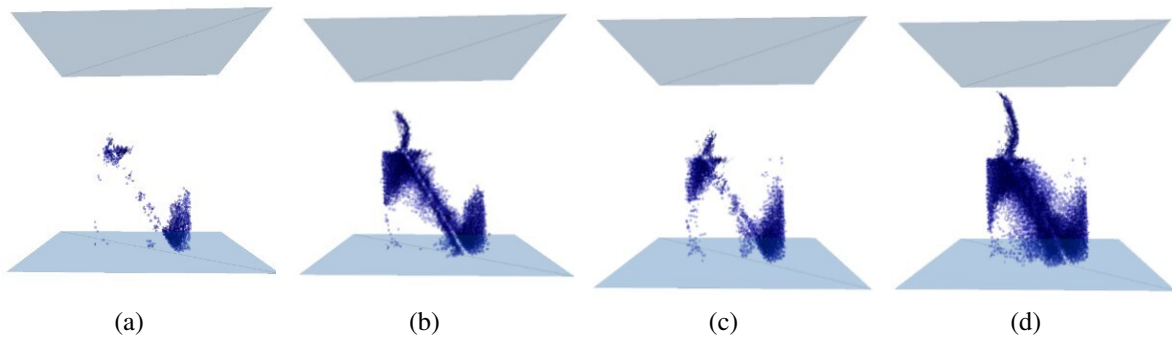


Fig. 13. Microcrack distribution of combination samples when $\theta = 60^\circ$. (a) Sample D at 3 minutes, (b) sample D at 7 minutes, (c) sample E at 3 minutes and (d) sample E at 7 minutes of loading.

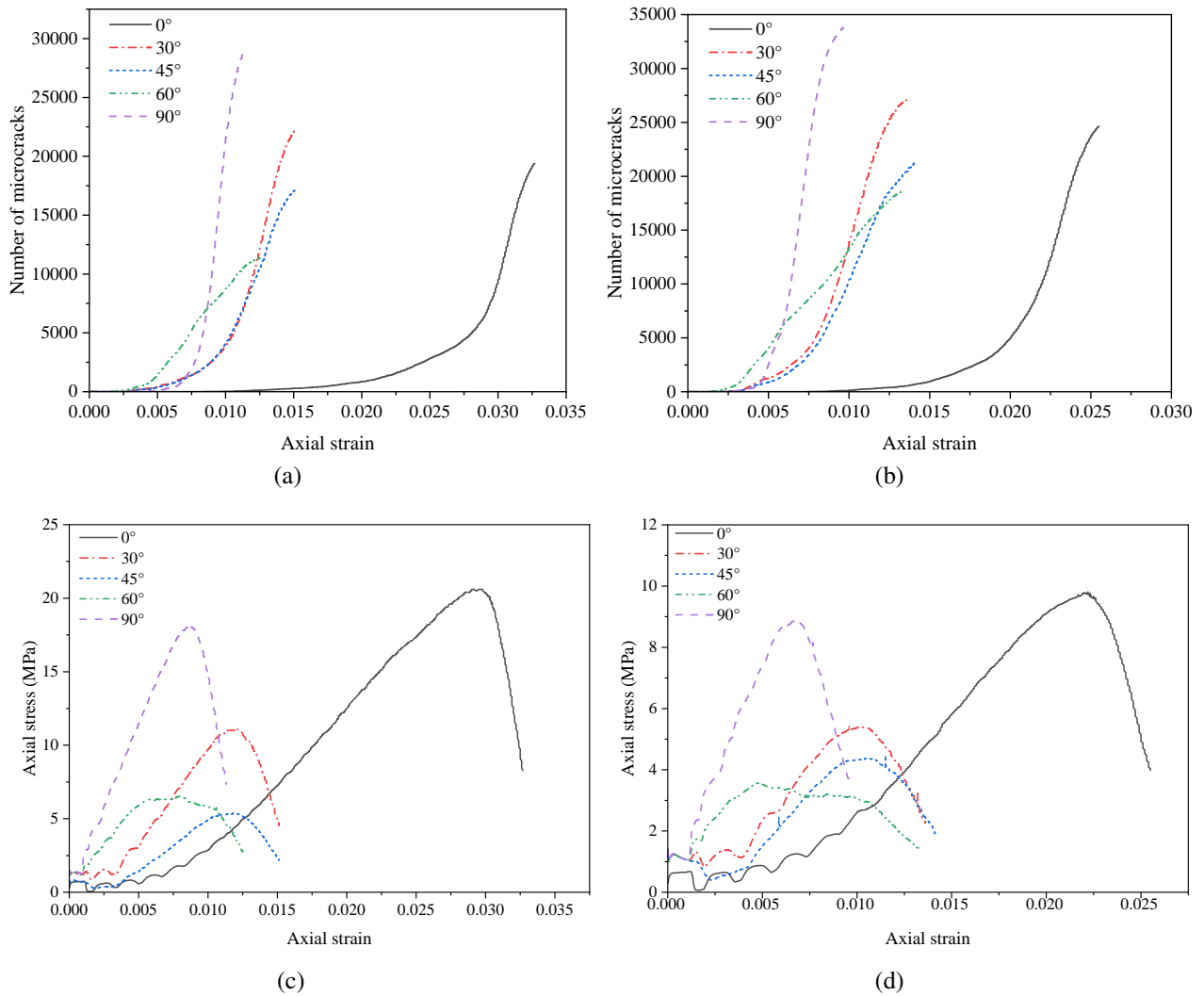


Fig. 14. Microcrack number and stress-strain curve of combination sample. (a) Microcrack number for sample D and (b) E; (c) Stress-strain curve for D and (d) E.

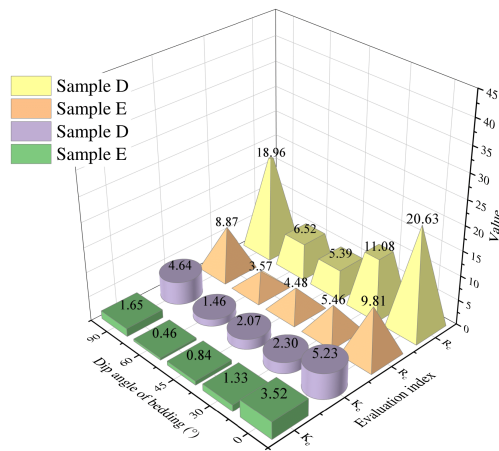


Fig. 15. R_c and K_e values of the combination samples.

sample bursting liability was comparative studied. The following primary conclusions could be drawn:

- 1) Four indexes, D_t , W_{et} , K_e , R_c , were selected to construct the judgment index system for coal bursting liability level, and a database containing 152 sets of coal samples with different bursting liability was established. Nine LightGBM classification models were built by combining three data preprocessing methods with three parameter optimization algorithms. After comparing the F1-score and stability of these nine models, the PSO-LightGBM classification model with Z-score normalization processing method was determined to be the optimal model with an F1-score of 93.6%.
- 2) Three types of coal samples with five dip angles were modeled and subjected to uniaxial compressive tests by PFC3D. The results showed that the uniaxial compression strength of samples first reduced and subsequently rose as the dip angle increased. Fragile failure was more common in the samples when the dip angle was either 0° or 90° . The development of microcracks was independent of the bedding planes and concentrated at the loading end. Shear and plastic failure were the main mechanisms of sample failure at 30° , 45° or 60° dip angles. Along the bedding planes, microcracks formed in accordance with the Jaeger's failure principle.
- 3) Numerical simulation studies involving uniaxial loads were conducted on coal-rock samples with five dip angles. It was concluded that the microcracks produced in samples were not aligned with the bedding planes whether the dip angle was 0° or 90° . Instead, their particles suffered severe damage and intersected to create larger fragmented blocks. In coal samples with dip angles of 30° , 45° or 60° , the failure mostly occurred along the bedding planes and their connecting ends.
- 4) Incorporating the R_c and K_e values of samples with different dip angles into the PSO-LightGBM model for coal and coal-rock samples, when the bedding dip angle was 0° or 90° , the bedding did not affect the bursting liability level of the samples.
- 5) The bedding impact varied in coal and coal-rock samples

with bursting liability. The impact of bedding and its dip angle should be taken into account when determining the bursting liability level. In addition, further investigations should be performed regarding the sample mechanical characteristics and the techniques for adjusting the bursting liability indices for samples with varying dip angles.

Acknowledgements

This research was supported by the National Natural Science Foundation of China (No. 42367024), the Key Laboratory of Mine Thermodynamic Disasters and Control of Ministry of Education (Liaoning Technical University) (No. JSK202207), the Major Science and Technology Special Project of Yunnan Province (No. 202202AG050014), and the Yunnan Innovation Team (No. 202105AE160023).

Conflict of interest

The authors declare no competing interest.

Open Access This article is distributed under the terms and conditions of the Creative Commons Attribution (CC BY-NC-ND) license, which permits unrestricted use, distribution, and reproduction in any medium, provided the original work is properly cited.

References

- Ali, M., Khan, N., Gao, Q., et al. Prediction of coal dilatancy point using acoustic emission characteristics: Insight experimental and artificial intelligence approaches. *Mathematics*, 2023, 11(6): 1305.
- Bentejac, C., Csorgo, A., Martinez-Munoz, G. A comparative analysis of gradient boosting algorithms. *Artificial Intelligence Review*, 2020, 54(2): 1937-1967.
- Bidgoli, M., Zhao, Z., Jing, L. Numerical evaluation of strength and deformability of fractured rocks. *Journal of Rock Mechanics and Geotechnical Engineering*, 2013, 6: 156-164.
- Chen, S., Zhao, Z., Feng, F., et al. Stress evolution of deep surrounding rock under characteristics of bi-modulus and strength drop. *Journal of Central South University*, 2022, 29(2): 680-692.
- Chiu, C., Wang, T., Weng, M., et al. Modeling the anisotropic behavior of jointed rock mass using a modified smooth-joint model. *International Journal of Rock Mechanics and Mining Sciences*, 2013, 62: 14-22.
- Frith, R., Reed, G., Jones, A. A causation mechanism for coal bursts during roadway development based on the major horizontal stress in coal: Very specific structural geology causing a localised loss of effective coal confinement and Newton's second law. *International Journal of Mining Science and Technology*, 2020, 30(1): 39-47.
- Hao, X., Yuan, L., Wang, S., et al. Study on bedding effect of bump tendency for hard coal. *Coal Science and Technology*, 2016, 46(5): 1-7. (in Chinese)
- He, S., Shen, F., Chen, T., et al. Study on the seismic damage and dynamic support of roadway surrounding rock based on reconstructive transverse and longitudinal waves. *Advances in Geo-Energy Research*, 2023a, 9(3): 156-171.

- He, S., Song, D., He, X., et al. Numerical modelling of rockburst mechanism in a steeply dipping coal seam. *Bulletin of Engineering Geology and the Environment*, 2023b, 82(7): 261.
- He, S., Song, D., Li, Z., et al. Precursor of spatio-temporal evolution law of MS and AE activities for rock burst warning in steeply inclined and extremely thick coal seams under caving mining conditions. *Rock Mechanics and Rock Engineering*, 2019, 52(7): 2415-2435.
- Inage, S., Ohgi, S., Takahashi, Y. Proposal and validation of an optimization method using Monte Carlo method for multi-objective functions. *Mathematics and Computers in Simulation*, 2024, 215: 146-157.
- Khan, N., Ahmad, M., Cao, K., et al. Developing a new bursting liability index based on energy evolution for coal under different loading rates. *Sustainability*, 2022, 14(3): 1572.
- Lambert, C., Coll, C. Discrete modeling of rock joints with a smooth-joint contact model. *Journal of Rock Mechanics and Geotechnical Engineering*, 2014, 6(1): 1-12.
- Li, Y., Wang, C., Liu, Y. Classification of coal bursting liability based on support vector machine and imbalanced sample set. *Minerals*, 2023, 13(1): 15.
- Liu, H., Li, X., Yu, Z. Influence of hole diameter on mechanical properties and stability of granite rock surrounding tunnels. *Physics of Fluids*, 2023, 35(6): 064121.
- Liu, X., Wang, X., Wang, E., et al. Effects of gas pressure on bursting liability of coal under uniaxial conditions. *Journal of Natural Gas Science and Engineering*, 2017, 39: 90-100.
- Mark, C., Gauna, M. Evaluating the risk of coal bursts in underground coal mines. *International Journal of Mining Science and Technology*, 2016, 26(1): 47-52.
- Melsom, B., Vennerod, C., de Lange, P. D., et al. Explainable artificial intelligence for credit scoring in banking. *Journal of Risk*, 2022, 25(2): 1-25.
- Mottahedi, A., Ataei, M. Fuzzy fault tree analysis for coal burst occurrence probability in underground coal mining. *Tunnelling and Underground Space Technology*, 2019, 83: 165-174.
- Mou, H., He, X., Song, D., et al. Response characteristics and influence mechanism of uniaxial compression mechanics and AE of coal with different joint angles. *Journal of China Coal Society*, 2020, 45(5): 1726-1732. (in Chinese)
- Muhammad, A., Wang, E., Li, Z., et al. Investigation of the acoustic emission and fractal characteristics of coal with varying water contents during uniaxial compression failure. *Scientific Reports*, 2023, 13(1): 2238.
- Park, B., Min, K., Thompson, N., et al. Three-dimensional bonded-particle discrete element modeling of mechanical behavior of transversely isotropic rock. *International Journal of Rock Mechanics and Mining Sciences*, 2018, 110: 120-132.
- Park, S., Jung, S., Jung, S., et al. Sliding window-based Light-GBM model for electric load forecasting using anomaly repair. *Journal of Supercomputing*, 2021, 77(11): 12857-12878.
- Peng, Y., Qiu, L., Zhu, Y., et al. Multi-scale multivariate detection method for the effective impact range of hydraulic fracturing in coal seam, *Journal of Applied Geophysics*, 2023, 215: 105124.
- Potyondy, D., Cundall, P. A bonded-particle model for rock. *International Journal of Rock Mechanics and Mining Sciences*, 2014, 41(8): 1329-1364.
- Qiu, L., Zhu, Y., Liu, Q., et al. Response law and indicator selection of seismic wave velocity for coal seam outburst risk. *Advances in Geo-Energy Research*, 2023, 9(3): 198-210.
- Saber, M., Boulmaiz, T., Guermoui, M., et al. Examining LightGBM and CatBoost models for wadi flash flood susceptibility prediction. *Geocarto International*, 2021, 37(25): 7462-7487.
- Sabzzadeh, I., Shourian, S. Maximizing crops yield net benefit in a groundwater-irrigated plain constrained to aquifer stable depletion using a coupled PSO-SWAT-MODFLOW hydro agronomic model. *Journal of Cleaner Production*, 2020, 262(1): 121349.
- Sakamoto, S., Ozera, K., Barolli, A., et al. Implementation of an intelligent hybrid simulation systems for WMNs based on particle swarm optimization and simulated annealing: Performance evaluation for different replacement methods. *Soft Computing*, 2019, 23(9): 3029-3035.
- Vardar, O., Wei, C., Zhang, C., et al. An energy-based quantitative coal burst proneness rating system for development roadways. *Geomechanics and Geophysics for Geo-Energy and Geo-Resources*, 2023, 9(1): 19.
- Vardar, O., Zhang, C., Canbulat, I., et al. A semi-quantitative coal burst risk classification system. *International Journal of Mining Science and Technology*, 2018, 28(5): 721-727.
- Yang, L., Wang, X., Li, J. Energy evolution and damage characteristics of coal with different bursting liability under uniaxial compression. *Coal Science and Technology*, 2021, 49(6): 111-118. (in Chinese)
- Yang, Z., Chen, J., Huang, T. Effect of joint sets on the strength and deformation of rock mass models. *International Journal of Rock Mechanics and Mining Sciences*, 1998, 35(1): 75-84.
- Zhang, Q., Wang, E., Feng, X., et al. Assessment of rockburst risk in deep mining: An improved comprehensive index method. *Natural Resources Research*, 2021, 30(2): 1817-1834.